

INSTABILITIES AND CLUMPING IN TYPE Ia SUPERNOVA REMNANTS

Chih-Yueh Wang and Roger A. Chevalier

Department of Astronomy, University of Virginia

P.O. Box 3818, Charlottesville, VA 22903-0818

`cw5b@virginia.edu, rac5x@virginia.edu`

ABSTRACT

We present two-dimensional high-resolution hydrodynamical simulations in spherical polar coordinates of a Type Ia supernova interacting with a constant density interstellar medium. The ejecta are assumed to be freely expanding with an exponential density profile. The interaction gives rise to a double-shocked structure susceptible to hydrodynamic instabilities. The Rayleigh-Taylor instability initially grows, but the Kelvin-Helmholtz instability takes over, producing vortex rings. Provided the simulation is initiated early in the evolution with a perturbation $\gtrsim 1\%$, the instability reaches its fully developed nonlinear strength within 5 doubling times. The further nonlinear evolution does not depend on the initial conditions. Considering the small initial radii of Type Ia supernovae, they are likely to reach this fully developed phase. The nonlinear instability initially evolves toward longer wavelengths and eventually fades away when the reverse shock front is in the flatter part of the supernova density distribution. Based on observations of X-ray knots and the protrusion in the southeast outline of Tycho's supernova remnant, we include clumping in the ejecta because these features cannot be explained by instabilities growing from small perturbations. The clump interaction with the reverse shock induces Rayleigh-Taylor and Kelvin-Helmholtz instabilities on the clump surface that facilitate fragmentation. In order to survive crushing and to have a bulging effect on the forward shock, the clump's initial density ratio to the surrounding ejecta must be at least 100 for the conditions in Tycho's remnant. The ^{56}Ni bubble effect may be important for the development of clumpiness in the ejecta. The observed presence of an Fe clump would then require a non-radioactive origin for this Fe, possibly ^{54}Fe . The large radial distance of the X-ray emitting Si and S ejecta from the remnant center indicates that they were initially in clumps.

Subject headings: hydrodynamics — instability — supernova remnants — supernovae: general — supernovae: individual (SN 1572)

1. INTRODUCTION

Type Ia supernovae (SNe) are thought to arise from the thermonuclear explosion of a white dwarf that accretes mass from its binary companion (Whelan & Iben 1973; Chevalier 1981a; Nomoto, Thielemann, & Yokoi 1984; Harkness 1991). Both Chandrasekhar and sub-Chandrasekhar mass models have been considered for the mass of the white dwarf at the time of the explosion. In the sub-Chandrasekhar mass models, He detonation occurs on the surface of the white dwarf (Woosley & Weaver 1994; Livne & Arnett 1995). Although these models have some attractive features, they seem less able than Chandrasekhar mass models to explain the light curves and spectra of Type Ia supernovae (e.g., Höflich & Khokhlov 1996). In Chandrasekhar mass models, ignition is initiated in the high density central regions of the white dwarf. In one type of model, the burning front propagates subsonically through the white dwarf. A popular example of this deflagration model is the W7 model of Nomoto et al. (1984), which can approximately reproduce the observed light curves. Branch et al. (1985) found that the model can reproduce the observed spectra if there is mixing of matter with a velocity $> 8,000 \text{ km s}^{-1}$, although Harkness (1991), in more detailed models, found that mixing may not be necessary. In another class of Chandrasekhar mass models, the initial subsonic burning front, or deflagration, makes a transition to a supersonic burning front, or detonation. This is the delayed detonation, or DD, model (Khokhlov 1991).

Although observations of extragalactic Type Ia supernovae have given insights into the nature of the explosions, a clear determination of the supernova model has not been possible. Observations of Galactic supernova remnants provide another window on the structure and composition of supernovae. Likely remnants of Type Ia explosions are Tycho’s supernova and SN 1006. Tycho’s supernova (SN 1572) appears to be a Type Ia supernova based on its reconstructed light curve (Baade 1945), although it may have been subluminous (van den Bergh 1993). Schaefer (1996) noted that the light curve allows a Type Ib origin, but the lack of evidence for stellar wind or photoionization effects in the surroundings of Tycho’s supernova argues against a massive star origin. At X-ray and radio wavelengths, Tycho shows a similar morphology, characterized by a limb-brightened circular shell. The outer edge is sharply defined and is interpreted as the forward shock front. Seward, Gorenstein, & Tucker (1983) found evidence for 400 X-ray clumps in the *Einstein* observatory image. At optical wavelengths, an $\text{H}\alpha$ emission filament, which is thought to be from a fast shock moving into a surrounding neutral material, is observed along the NE perimeter, supporting the shock interpretation. The remnant outline spans $8'$ in diameter, corresponding to a linear radius of $\sim 3 \text{ pc}$ for an assumed distance of 2.5 kpc (Raymond 1984). The HI absorption show that the environment surrounding Tycho is fairly uniform, without a prominent density gradient (Reynoso et al. 1999). This property makes it especially suitable for detailed study.

Hamilton et al. (1986) calculated a one-dimensional hydrodynamical model to study the X-ray spectrum of Tycho’s remnant and obtained good agreement with spectra from the *Einstein* Observatory and other X-ray observatories. They took a three-layer composition structure and were successful in reproducing the observed Si line emission. However, they chose a constant density profile for the supernova. When this type of supernova density profile interacts with a

constant density ambient medium, the outer shocked layers (where Si was placed in the model) end up dense and cool. A constant density profile is probably a poor representation of an exploded Type Ia supernova. Dwarkadas & Chevalier (1998, hereafter DC98) recently reviewed the types of explosion models that reproduce the basic properties of Type Ia supernovae and found that an exponential profile is the best approximation for the density profile overall, although there can be significant deviations from this profile. When such a profile interacts with a constant density medium, the shocked supernova gas has an approximately constant temperature. In order to reproduce the observed spectral properties of Tycho’s remnant, DC98 suggested that either the supernova gas has dense clumps or there was an early phase of interaction with a circumstellar medium. This was on the basis of one-dimensional hydrodynamic models for the interaction of a Type Ia supernova with a surrounding medium.

In order to make further progress, we extend the hydrodynamic modeling effort to two dimensions. One motivation for this is the investigation of instabilities that result from the deceleration of the supernova ejecta by the ambient medium. Chevalier, Blondin, & Emmering (1992) previously investigated the interaction of a power law supernova density profile with an ambient medium. In this case, the flow approaches a self-similar state, although turbulent motions are continuously fed by the instability. In the case of an exponential profile, the flow is no longer self-similar; the density profile effectively evolves from a steep power law profile to a flatter one. Chevalier et al. (1992) investigated the instability for a range of power law indices and found that the flow remained qualitatively similar. In view of this, we expect the exponential case to be qualitatively similar while the steep part of the density profile is interacting with the surroundings, even though the flow is no longer self-similar. Our aim is to determine the nature of the evolution. Dwarkadas (2000) has already made some numerical studies of this phenomenon.

Another part of our effort is to include density inhomogeneities in the freely expanding supernova gas. The *ASCA* observatory has made possible the imaging of Tycho’s remnant in moderately narrow X-ray bands (Hwang & Gotthelf 1997). There are two X-ray emitting knots on the eastern side of the remnant where there is a protrusion in the remnant’s outline (Vancura et al. 1995; Hughes 1997; Hwang & Gotthelf 1997). One of these knots is strong in Si line emission and the other is strong in Fe line emission. With the *ROSAT* HRI, Hughes (1997) has measured the proper motion of features in the X-ray emission. He found that these two knots show approximately undecelerated motion. On the other hand, radio observations over the whole remnant show substantial deceleration, with $Vt/R \approx 0.47$ (Reynoso et al. 1997 and references therein), where V is the shock velocity and R is the radius. The implication is that the knots represent not only an inhomogeneous composition, but also higher density clumps that have not been decelerated. At a distance of 2.5 kpc, the velocities of the knots are about 8,300 km s⁻¹ (Hughes 1997).

The other well observed Type Ia supernova remnant, SN 1006, does not show evidence for the expansion of X-ray emitting clumps. However, absorption line studies of the Schweizer-Middleditch star behind the remnant have provided a powerful probe of the supernova remnant structure and composition (Wu et al. 1983, 1997; Fesen et al. 1988). These observations show evidence for central

cool Fe II that is compatible with expectations for the unshocked Fe rich matter in the central region of a Type Ia supernova, although the amount of Fe is smaller than expected (Hamilton et al. 1997 and references therein). In addition, there is evidence for Si II absorption that is redshifted over the velocity range $3,000 - 7,000 \text{ km s}^{-1}$ (Wu et al. 1997; Hamilton et al 1997). Fesen et al. (1988) initially argued that the Si rich matter is in a clump on the far side of SN 1006. However, Hamilton et al. (1997) more recently argued for a spherically symmetric model for the supernova ejecta in which there is a transition from Fe to Si rich gas at a velocity of $5,600 \text{ km s}^{-1}$ and the supernova remnant is considerably more extended on the back side because of a low interstellar density in that direction. They argue against a Si clump, but appear to assume that the clump gas would have been shocked and cooled. Another possibility is that low ionization absorption is due to unshocked matter in the clump. The clump may be moving at about $7,000 \text{ km s}^{-1}$ and matter stripped from the clump may lead to the matter extending to lower velocities. The remnant can then have a shape that is closer to spherical symmetry; the presence of a clump implies that the ejecta are not in spherical shells, but this is also indicated in Tycho’s remnant.

Our aim here is to examine how inhomogeneities in the ejecta interact with the decelerated interaction region. The observed properties can place constraints on the nature of the inhomogeneities, which can be important for the explosion models.

The plan of our paper is as follows. In § 2, we discuss the density structure of a Type Ia supernova and consider mechanisms that might give rise to inhomogeneities in the ejecta. Our method is given in § 3. Results on the growth of instabilities from small perturbations are in § 4. The evolution of nonlinear inhomogeneities is given in § 5. Our results are discussed in the context of observations of Tycho’s supernova remnant in § 6. Implications for models for Type Ia supernovae are in § 7 and the conclusions are in § 8.

2. DENSITY STRUCTURE IN TYPE Ia SUPERNOVAE

Soon after a supernova explosion, the ejecta are expected to be freely expanding, with velocity $v = r/t$. In this phase, DC98 found that an exponential density profile generally describes the density distribution obtained from numerical 1-D (one-dimensional) explosion models, including delayed detonation, pulsating delayed detonation, He detonation, and deflagration models. The exponential density profile is given by

$$\rho_{SN} = A \exp(-v/v_e) t^{-3}, \quad (1)$$

where A is a constant and v_e is the velocity scale height, which is determined by the total ejecta mass M and explosion energy E . This expression allows for spherical expansion; an element of supernova gas moves with a constant velocity and has its density drop as t^{-3} . Integrating the density and energy density over space and time gives (DC98)

$$M = 4\pi A v_e^3, \quad E = 48\pi A v_e^5, \quad (2)$$

or

$$v_e = (E/6M)^{1/2} = 2.44 \times 10^8 E_{51}^{1/2} \left(\frac{M}{M_{ch}} \right)^{-1/2} \text{ cm s}^{-1}, \quad (3)$$

$$A = \frac{6^{3/2} M^{5/2}}{8\pi E^{3/2}} = 7.67 \times 10^6 \left(\frac{M}{M_{ch}} \right)^{5/2} E_{51}^{-3/2} \text{ g s}^3 \text{ cm}^{-3}, \quad (4)$$

where $M_{ch} \equiv 1.4M_\odot$ is the Chandrasekhar mass and E_{51} is the explosion energy in units of 10^{51} ergs. A larger ratio of E/M gives a larger velocity scale height and produces a flatter density profile at a given velocity.

In some Type Ia models and core collapse models, the outer density distribution has been described by a power law. Then, the ejecta density is given by $\rho \propto v^{-n}t^{-3}$, where $v = r/t$ and n is a constant > 5 . If the ejecta interact with a shallow power law medium $\rho \propto r^{-s}$ with $s < 3$, there exist self-similar solutions for the shocked flow (Chevalier 1982a). The problem contains only two independent dimensional parameters: the coefficients of the supernova density and the external density. In the exponential case there is an additional parameter, the velocity scale height v_e , so that the problem is not self-similar.

The exponential profile is an oversimplification of the density profile, as can be seen in fig. 1 of DC98. In a thermonuclear explosion, the elements of gas receive most of their energy from the burning of that gas, as opposed to a shock wave as in the case of core collapse supernovae. The expansion of these heated elements is what leads to the approximately exponential density distribution. If there is incomplete burning of the material, the internal energy per unit mass of the gas is lower than in neighboring regions where complete burning has taken place. The gas is expected to evolve toward pressure equilibrium, compressing the incompletely burned region. The magnitude of the effect can be estimated by considering the relative energy densities produced by different burning processes, and allowing the gas with the greater burning to adiabatically expand to come into pressure equilibrium with the other gas. The difference in burning a C/O mixture to Si or to Ni does not lead to a large density difference: $\lesssim 40\%$ higher density in the Si gas. We will find that this is not sufficient to explain the clumping indicated in Tycho's remnant. If some C or O is left unburned, a greater degree of compression is expected, but this typically applies to only the outermost layers of the supernova. This effect can apparently be seen in models (e.g., the W7 model density distribution shown in Fig. 1 of Branch et al. 1985).

On a longer timescale, the density structure can be changed by the Ni bubble effect. The occurrence of SN 1987A brought the realization that the energy release by radioactive ^{56}Ni and ^{56}Co after the initial explosion could affect the density and composition structure within the supernova (e.g., Woosley 1988). Li, McCray, & Sunyaev (1993) analyzed the Fe/Ni/Co lines from SN 1987A and showed that the filling factor of Fe with velocity $\lesssim 2500 \text{ km s}^{-1}$ was $\gtrsim 0.3$ although the mass fraction of this element was only ~ 0.01 in the same region. They attributed this effect to the expansion of gas heated by radioactive power deposition. Basko (1994) made more detailed calculations of the expansion effect. Li et al. (1993) noted that the structure should show up in young supernova remnants and briefly mentioned the Crab Nebula. Chevalier (2000) contrasted

the operation of the effect in Type Ia and in core collapse supernovae, and we follow his discussion of the Type Ia events here.

We examine the expansion of a spherical volume of radioactive gas, following Basko (1994). To get a crude estimate of the effect, we assume that immediately after the explosion, the supernova gas is freely expanding and has constant density throughout. The velocity at the edge of a spherical clump of ^{56}Ni with mass M_{Ni} is

$$U_0 = 7.7 \times 10^3 \left(\frac{M_{\text{Ni}}}{0.5 M_\odot} \right)^{1/3} \left(\frac{E}{10^{51} \text{ ergs}} \right)^{1/2} \left(\frac{M}{M_{\text{ch}}} \right)^{-5/6} \text{ km s}^{-1}. \quad (5)$$

The deposition of radioactive energy in the ^{56}Ni gas leads to expansion so that the velocity of the outer edge of the region becomes U_∞ . Conservation of energy leads to the equation

$$X^5 - X^2 = \frac{5Q}{U_0^2}, \quad (6)$$

where $X = U_\infty/U_0$ and Q is the energy per gram deposited by radioactivity. The assumption of full deposition of energy in the gas implies $Q = 3.69 \times 10^{16} \text{ ergs g}^{-1}$ for $^{56}\text{Ni} \rightarrow ^{56}\text{Co}$ and $Q = 7.87 \times 10^{16} \text{ ergs g}^{-1}$ for $^{56}\text{Co} \rightarrow ^{56}\text{Fe}$. The expansion is limited by the diffusion of either the γ -rays or the photons out of the high pressure bubble so that the full values of Q listed above may not be achieved. The bubble expansion is expected to drive a shell in the incompletely burned matter on the outside. Basko (1994) showed that the shell is subject to the Rayleigh-Taylor instability, but that the instability does not have much effect on the shell expansion. The shell may break into clumps. Equation (6) shows that if U_0 is large, the expansion of the Ni bubble is relatively small and the factor increase in the filling factor (X^3) is small. Clumps can still be created in the swept up gas. On the other hand, small regions of ^{56}Ni have the potential to substantially increase their filling factor in the supernova gas.

The reference values used in equation (5) are those thought to be typical of Type Ia supernovae. These supernovae typically reach maximum light on a timescale of 15 days. This is the timescale on which diffusion of the internal radiative energy becomes effective, which has the effect of smoothing pressure gradients and stopping Ni bubble expansion. The mean life of ^{56}Ni is 8.8 days and that of ^{56}Co is 114 days, so we estimate that the ^{56}Ni radioactive energy is deposited in the radioactive gas, but not that from ^{56}Co . After the expansion due to the radioactivity, the outer velocity of the Fe-rich region is $8,400 \text{ km s}^{-1}$ and about $0.13 M_\odot$ of matter has been swept into a shell around the Fe-rich region. These numbers are approximate and will change for the density profile of a specific supernova.

As discussed in § 1, Tycho’s remnant shows evidence for two knots that have moved with undecelerated motion. At a distance of 2.5 kpc, the velocities of the knots are about $8,300 \text{ km s}^{-1}$ (Hughes 1997). This velocity is consistent with that expected in a clumpy shell formed by the expansion of radioactive gas. However, Fe is expected in a clump only if it formed as non-radioactive Fe. The Fe clump may have formed as ^{54}Fe . X-ray spectra of Tycho’s remnant have been obtained

with the result that, in general, Fe line emitting gas is at a higher temperature and lower density than Si line emitting gas (Hwang, Hughes, & Petre 1998 and references therein). This is also expected as a result of the Ni bubble effect.

These considerations show that there is some evidence in Type Ia supernova remnants for clumping surrounding a large Ni bubble. The agreement between the knot velocities in Tycho’s remnant and those expected for the Ni bubble shell is probably fortuitous. There is some evidence for both Tycho and SN 1006 that they were subluminous supernovae (e.g., van den Bergh 1993; Schaefer 1996), which would imply a smaller amount of ^{56}Ni . For the subluminous Type Ia SN 1991bg, Mazzali et al. (1997, and references therein) estimate the synthesis of $0.07 M_{\odot}$ of ^{56}Ni extending to a velocity of $5,000 \text{ km s}^{-1}$. This mass is consistent with the upper limit on the Fe mass ($< 0.16 M_{\odot}$) found by Hamilton et al. (1997) for SN 1006.

The density contrast that is created by the nickel bubble is not well determined. In the calculations of Basko (1994), the density contrast at the edge of the bubble is a factor ~ 5 above the surroundings. However, in the case of a Type Ia supernova with a relatively much greater amount of radioactive Ni, clumps of non-radioactive material may be immersed in the radioactive Ni and subjected to a greater compression (Höflich 2000). We have considered a simple model for this process in order to estimate the compression. We assume that the expanding supernova gas has a constant density and that the free expansion during the first day is negligibly affected by the addition of energy, as above. The energy equation can be written as

$$\frac{1}{\gamma - 1} \frac{dpV}{dt} = \frac{dQ}{dt} - p \frac{dV}{dt}, \quad (7)$$

where γ is the adiabatic index, V is the volume, and dQ/dt is the heat addition from radioactivity. Over most of the evolution, the gas is radiation dominated and $\gamma = 4/3$, although the thermal pressure may be significant in the initial phases. Provided $t \lesssim 1$ day, the power input from ^{56}Ni is approximately constant at $4.8 \times 10^{10} \text{ ergs g}^{-1} \text{ s}^{-1}$. Consideration of eq. (7) shows that in non-radioactive gas the pressure falls as t^{-4} ; this also initially applies to the radioactive gas, but it switches to t^{-2} evolution (at $t \approx 2 \times 10^3 \text{ s}$ for typical parameters). If the radioactive gas can keep non-radioactive gas at its pressure, the compression of the non-radioactive gas increases as $t^{3/2}$ and can reach ~ 200 after a day. However, a typical clump cannot be maintained in pressure equilibrium at the high pressure and a compression wave is driven into the clump from the outside. When the radiative diffusion timescale becomes less than the age, there is the possibility that the gas is more compressible and larger density inhomogeneities are created. This effect has been found in calculations of shock breakout from a star in supernova models (e.g., Chevalier 1981b). An important aspect of the effect is that radiation pressure dominates the gas pressure, which is the case here. These issues will have to be examined in detailed computations.

This discussion shows that it is possible that Type Ia supernovae do contain inhomogeneities which could be observed in a supernova remnant. The Ni bubble effect occurs on a timescale of 10 days, or a scale of 10^{15} cm for a velocity of 10^4 km s^{-1} . The structure resulting from the Ni bubble should become frozen into the ejecta at this early time.

3. METHOD

We used the 2-D (two-dimensional) code ZEUS2D based on a finite difference scheme to carry out the hydrodynamical simulations (Stone & Norman 1992). The code uses an artificial viscosity to smooth shock transitions. We first ran 1-D simulations with an inner exponential density profile (ejecta) interacting with an outer constant density ambient medium, starting 2 weeks after the supernova explosion. The initial density distribution evolved into an intershock structure consisting of reverse-shocked ejecta in the inner region and a forward-shocked ambient medium on the outside, separated by a contact discontinuity (DC98). The 1-D intershock profile was then used to initiate 2-D simulations. The inner ejecta gas was freely-expanding, using an inflow boundary condition. The outer gas was at rest. Gas pressure in the unshocked gas was unimportant. We neglected the effects of magnetism, heat conduction, and radiation. Magnetic fields may play a role in suppressing heat conduction and viscosity, but are not expected to be dynamically significant in the supernova remnant. The radiative cooling time for the optically thin gas at an age $\lesssim 300$ yrs is greater than the age of the remnant. We assumed that the energy losses through X-ray emission are small so that the dynamics of the flow are not affected by gas cooling. We used an adiabatic index $\gamma = 5/3$.

In 1-D runs, the starting dynamical age determines the initial ejecta-ISM interface position. Simulations with different initial ages showed that the evolution quickly converges within a few radial doubling times. The solution is unique, independent of when the simulation starts (see DC98). More generally, since the ejecta density profile only depends on its explosion mass and kinetic energy, the interaction with an ambient medium can be described by a set of scaling parameters R' , V' , T' using M , E , and ρ_{am} (see Truelove & McKee 1999; DC98)

$$R' = \left(\frac{3M}{4\pi\rho_{am}} \right)^{1/3} \approx 2.19 \left(\frac{M}{M_{ch}} \right)^{1/3} n_0^{-1/3} \text{ pc}, \quad (8)$$

$$V' = \left(\frac{2E}{M} \right)^{1/2} \approx 8.45 \times 10^3 \left(\frac{E_{51}}{M/M_{ch}} \right)^{1/2} \text{ km s}^{-1}, \quad (9)$$

$$T' = \frac{R'}{V'} \approx 248 E_{51}^{-1/2} \left(\frac{M}{M_{ch}} \right)^{5/6} n_0^{-1/3} \text{ yr}, \quad (10)$$

where $n_0 = \rho_{am}/(2.34 \times 10^{-24} \text{ gm cm}^{-3})$ and ρ_{am} is the ambient density. The dimensional variables r , v , t can be expressed in terms of the nondimensional quantities: $r' = r/R'$, $t' = t/T'$, and $v' = v/V'$. Nondimensional solutions can be conveniently returned to dimensional ones by re-scaling, and new dimensional solutions for different M , E , and ρ_{am} can be calculated. For a particular density distribution, one evolutionary sequence in the nondimensional variables represents all possible dimensional solutions.

For the exponential density profile, the 1-D solution (Fig. 1) entered the Sedov-Taylor self-similar blast wave evolution with $r \propto t^{0.4}$ at $t' \gg 1$. As the ejecta density decreased with time, the reverse shock, initially moving outward in the stellar frame, began to move inward at $t' \approx 2.5$. It reached the stellar center at $t' \approx 8$.

4. INSTABILITIES FROM SMALL PERTURBATIONS

We simulated the Rayleigh-Taylor instabilities in the intershock region in two-dimensional spherical polar coordinates assuming ϕ -symmetry. The 2-D numerical grid was initialized with the 1-D solution at $t' = 0.00054$ (0.134 yrs for the standard parameters $E_{51} = 1$, $M = M_{ch}$, and $n_0 = 1$) across the angular domain, with perturbation seeds in density, pressure, and velocity placed between the contact discontinuity and the reverse shock wave. The grid was radially expanding, following the intershock boundaries until the reverse shock radius turned over to the stellar center. The evolution was tracked for five orders of magnitude in time. Simulations initiated earlier presented numerical problems because the higher density contrast across the contact discontinuity reduced the numerical time step determined by the Courant condition. The 2-D grid was moved based on the 1-D results. We used grid wiggling in the 1-D simulations, tracking the forward and the reverse shocks. In this process, the grid expands and contracts so that the shock locations are kept at the same grid numbers. We fit the evolution of the radii and velocities with a linear function and a logarithmic polynomial, respectively. We then applied the 1-D smooth fits on the 2-D grid boundaries, avoiding significant numerical noise coming from the wiggling scheme. The radial zone boundaries had a velocity distribution linearly varying with distance to the inner boundary, so that the zone spacing was kept uniform during the expansion. We used 500 zones in the radial direction and varied the number of angular zones; the radial zone spacing was $3 \times 10^{-6} R'$ at $t'=0.01$, and increased to $1.6 \times 10^{-3} R'$ at $t'=1.73$.

We investigated the growth of instabilities with various grid resolutions and perturbations. To reduce the computational expense, only a fraction of a quadrant centered at $\theta = 45^\circ$ was used. The run with the finest resolution had 2000 angular zones in 1/2 of a quadrant. The radial boundary conditions were inflow and outflow at the inner and outer sides, respectively. The angular boundaries were reflecting. We generally used a spherical harmonic function for the perturbation,

$$Y_{lm}(\theta, \phi) = P_l^m(\cos \theta)e^{im\phi}, \quad (11)$$

where $m = 0$ and the harmonic l (perturbation mode) is even, considering the ϕ -symmetry and the reflection symmetry about the equator. The angular perturbation is essentially the associated Legendre polynomial P_l^m , which has an increasing amplitude toward the polar axis. We applied perturbations such that the amplitude was between 1% and 50% near $\theta = 45^\circ$. The perturbed width was less than 40% of the distance between the reverse shock and the contact discontinuity, about 2.5% of the whole intershock width.

4.1. Evolution

Fig. (8) illustrates the evolution of the instability perturbed by a 1%, $l = 100$ mode using 2000 angular zones on 1/2 of a quadrant centered on $\theta = 45^\circ$. Small perturbations in the density grow and form spikes that protrude from the contact discontinuity into the forward-shocked region. As

the remnant expands, the Rayleigh-Taylor instabilities continue to grow to form mushroom-shaped caps while the stems become narrower. Secondary fingers develop at the same time, so that there are more fingers than the initial perturbation mode suggests. After reaching their maximum extent, the fingers fall to their sides and interfere with neighboring fingers. The forward growth of the caps is blocked by the drag of the flow and the fingers do not extend farther from the dense shell at the contact discontinuity.

In the later stages, the Kelvin-Helmholtz instability takes over at the mushroom caps, creating vortex rings. The relative motion of flows between a finger and its surroundings bends the stem and disrupts the flow. Since the effect of drag increases as the finger grows outward, the continual shedding of mass at the finger’s top eventually leaves insufficient mass to overpower the drag of the countersteaming flow. The mushroom cap falls off to the side, and the remaining filaments are swept back. Vorticity develops in the less dense regions left by the original mushroom caps. Globally, the vortex rings gradually come to dominate over the spikes, and only the stems remain recognizable.

The Rayleigh-Taylor instability consistently builds up fingers with long wavelengths (low l). The dynamical stages of evolution can thus be distinguished by the dominant mode. We found four stages of evolution. The first stage is characterized by linear growth of the Rayleigh-Taylor instability; the perturbations grow out from the initial seeds and evolve towards a mushroom shape. Second, nonlinear growth of secondary fingers among primary ones becomes important. The fingers multiply and become congested. Third, mutual interference among fingers increases the wavelength of the dominant mode; vortex rings develop as the Kelvin-Helmholtz instability becomes active, although new fingers still develop, as in a convective roll. The instability is fully developed at this point. In the final stage, the intershock density contrast is reduced as the expansion decelerates; vortex rings and all the other features in the flow are dispersed, and the instabilities fade.

Figs. (3) and (4) show the angle-averaged density profiles with various resolutions at an early phase and at $t' = 1.6$ (approximately the present epoch for Tycho). Compared to the 1-D solution, the reverse shock front smears out somewhat because it is corrugated, and the density peak at the contact discontinuity is not present. The forward shock front is less affected. Various resolutions give basically the same profile, although finer grid resolutions reveal larger fluctuations. The late phase shows less density contrast and the decline of instabilities.

We compare the exponential case to the power law case of $n = 7$ with $s = 0$ (interstellar medium) and $s = 2$ (circumstellar wind) in Chevalier et al. (1992). In the power law case, the conditions are self-similar, so that the evolution is quasi-steady. Convection cells continually stir up a region near the contact discontinuity. The density structure remains qualitatively similar with time. The difference in the two $n = 7$ cases with different ambient media is that for the $s = 2$ case the density structure is characterized by groups of slender blobs with a pyramid outline, while for the $s = 0$ case it is characterized by individual mushroom shapes. The reason is that a constant density surrounding medium causes a smaller density contrast across the the unstable region, and

a negative gradient of entropy. Thus, the $s = 2$ case allows the initial blobs to grow and stretch out into narrow fingers, contrary to the $s = 0$ case in which the flow is blocked from propagating further and ends in a mushroom cap.

The $s = 0$ power law case studied by Chevalier et al. (1992) shows that a larger power law index n increases the dominant mode l and the evolution goes from quasi-steady convection to intermittent growth of slender fingers, approaching in a sense the general profile of the low- n , $s = 2$ cases. This is due to the larger density contrast between the shocked ambient medium and the shocked ejecta at larger n , and to the fact that the gradients in the shocked ambient region become shallower. The exponential case exhibits evolutionary properties similar to the power law case with decreasing index with time, in that longer wavelengths are built up throughout the evolution after the initial growth stage.

We show in Fig. (5) the approximate power law index $n_{ej} = -d \ln \rho / d \ln r$ in the unshocked ejecta just inside the reverse shock for the exponential case. In the 2-D simulations, the reverse shock surface is corrugated, but its position does not deviate significantly from its position in the 1-D case. The position of the contact discontinuity found by dimensional analysis is $R_c \propto t^{(n-3)/(n-s)}$ for a power law ejecta density profile and an ambient medium $\rho \propto r^{-s}$. The power law index for $n = 5$ is the same as that for a Sedov-Taylor blast wave. For $n \leq 5$ the forward shock is still expected to expand with the Sedov law; however, the contact discontinuity expands more slowly than $r \propto t^{0.4}$ and steadily distances itself from the forward shock in the self-similar frame (Chevalier 1982a). Self-similar solutions are no longer possible and the reverse shock starts to move inward towards the center. For the exponential case, we expect that the deceleration at the contact discontinuity is reduced when the reverse shock is in ejecta with $d \ln \rho / d \ln r \leq 5$. The instabilities should then lose the deceleration that drives them. The index n starts to fall below 5 at $t' \geq 0.325$, while the turnover of the reverse shock actually occurs at $t' \sim 2.5$; the motion of the reverse shock takes time to respond to the changing density profile.

Both the density contrast and acceleration decline rapidly with time in the exponential case; the decline of the instabilities is an inevitable consequence. At the end of our simulation ($t' = 2.16$), there is little continuing development of the instability.

4.2. Variation of the Perturbation and the Resolution

The evolution of the instability is insensitive to the initial linear perturbation. We have applied the initial perturbation in various areas: between the contact discontinuity and the forward shock, ahead the forward shock, and inside the reverse shock. After the growth stage, the sizes of the unstable regions are similar in all the cases. Perturbations placed at the shocked ejecta near the contact discontinuity are the most effective in exciting the instability.

On a low resolution grid of 500×200 zones on $1/2$ of a quadrant, a 10% perturbation with $l = 100$ initially has 12 Rayleigh-Taylor fingers, which subsequently double in number. The $l = 50$

mode generates three secondary fingers between every two primary fingers, resulting in 24 fingers like the $l = 100$ mode (Fig. 8). There appears to be a preferred mode shortly after the linear growth, independent of the initial conditions. However, with finer resolution more details between the primary fingers appear and the presence of a dominant mode becomes vague. More highly resolved fingers appear to be more slender and sharp, and the overall flow patterns thus appear different. On finer grids, the flow pattern approaches the pyramid shape of an $n = 7$, $s = 2$ power law density case; mushroom structures become congested and twisted at the base near the contact discontinuity. Toward the end of the evolution, a preferred mode in increasing wavelength is built up independent of grid coarseness or the initial conditions. The presence of the late-stage dominant mode can be understood as the exponential model having a continually decreasing power law index, although limited resolution can also fabricate a longer wavelength dominant mode. Our results are consistent with the studies of Rayleigh-Taylor instability growth in a stellar explosion by Fryxell, Müller and Arnett (1991), who used a PPM (piecewise parabolic method) code and cylindrical coordinates.

The morphology of the fingers on our higher resolution runs is similar to that of Kane, Drake, & Remington (1999) using the PPM code PROMETHEUS. The results of Chevalier et al. (1992) using the piecewise parabolic code VH-1, Jun & Norman (1996a) using ZEUS2D, and Fryxell et al. (1991) using PROMETHEUS appear to have lower resolution than our results and do not show the narrow structure that we find. The high resolution calculation of Müller, Fryxell, & Arnett (1991) is closer to the morphology that we obtain. Higher resolution calculations introduce shorter wavelength numerical noise and allow small perturbations to develop. Small scale structures have a faster growth rate of the Rayleigh-Taylor instability in the linear regime, and this can be seen in our simulations. Fig. (8) shows that the initial growth of Rayleigh-Taylor fingers leads to fingers with a larger extent at high resolution, presumably because the smaller cross section gives less drag. However, this trend may begin to reverse at the highest resolution because the stems of the Rayleigh-Taylor fingers become more unstable (see $t' = 0.003$ in Fig. 8). As mentioned above, the extent of the unstable region shows little dependence on resolution in the fully developed regime. On finer grids, the fingers in the nonlinear regime show an increasing tendency to bend, which prompts stronger interaction among fingers and produces more complex structures. As the resolution increases, the mushroom caps break up into filaments; this trend continues at our highest resolution. The clear mushroom shapes found in lower resolution calculations may be an artifact of the limited resolution.

In independent work that was concurrent with our study, Dwarkadas (2000) simulated the instabilities resulting from the interaction of supernova ejecta (with an exponential profile) with a surrounding medium. He presented the evolution of the instability for a case in which it grew from numerical noise. This perturbation is much smaller than the cases that we considered and the instability remained in the linear regime until the late damping stage of the instability. When he initiated the simulations with a 2 % perturbation, his results are consistent with ours.

We have also simulated the evolution for an initial perturbation with 100% amplitude. After

a transition phase during which the intershock region became more than twice as broad as in the standard case, the evolution returned to the standard case. As found by Kane, Drake, & Remington (1999) in simulations with a power law supernova density profile, the standard evolutionary track is robust.

5. EVOLUTION OF CLUMPS

As discussed in § 1, recent X-ray (Hughes 1997; Hwang & Gotthelf 1997) and radio (Velázquez et al. 1998) observations of Tycho’s remnant show two knots juxtaposed near the eastern edge. The outer outline of radio (Velázquez et al. 1998) and X-ray (Vancura et al. 1995) emission, which presumably defines the forward shock front, shows an outward protrusion surrounding the knots. The properties of undecelerated motion (Hughes 1997) and an outer shock protrusion cannot be explained by instabilities generated by linear perturbations. The Rayleigh-Taylor fingers from linear perturbations are substantially decelerated and do not affect the outer shock front. Although our computations are two-dimensional, we believe that going to three dimensions would not change this conclusion. Rayleigh-Taylor fingers are known to show somewhat greater growth in three dimensions during the initial growth phase (e.g., Kane et al. 2000 and references therein). However, in computations with power law supernova ejecta, Jun & Norman (1996b) find that the thickness of the mixing layer is very similar in two and three dimensions when the instability is fully developed (see their figs. 2 and 3). The instability is probably limited by the properties of the interaction region. Jun & Norman (1996b) do find that the stellar ejecta show smaller scale structure in three dimensions.

We believe that the origin of the knots is best explained by nonlinear clumps of supernova ejecta expanding into the intershock region. We thus simulated the hydrodynamic evolution of ejecta clumps interacting with the intershock gas. We represented clumps as denser spheres superposed on the smooth exponential density profile. In the simulations, we initialized a clump at the polar angle $\theta = 45^\circ$ on 2-D computations like those described in the previous section. In two dimensions, the sphere is in fact a 3-D torus around the polar axis. A 3-D sphere can be simulated by placing the clump on the polar axis $\theta = 0$ on a 2-D grid; however, there are then singularity problems on the symmetry axis of the grid, which lead to long Rayleigh-Taylor fingers on the axis due to the instabilities discussed in the previous section. Comparisons of the hydrodynamics of ISM clouds in spherical and toroidal morphologies indicate that geometry contributes little to the interaction (Jun & Jones 1999). To examine the effect of geometry, we carried out clump interaction simulations with clumps at $\theta = 15^\circ$ and $\theta = 80^\circ$; the clump evolution did not substantially change.

Under the same boundary conditions as used for the instability computations, the clump was included in the freely expanding ejecta. The clump first ran into the reverse shock and then moved forward through the intershock region. The initial clump as well as the ejecta were cold compared to the high temperature shocked ejecta. The gas pressure was unimportant, so that the size and the density contrast of the clump remained unchanged until the clump expanded into the reverse

shock front.

The basic physics of the interaction is similar to that for the interaction of nonradiative blast waves with an interstellar cloud (Klein et al. 1994). As the shock wave moves past the cloud, a reflected wave moves back into the shocked intercloud gas and creates a bow shock. The incident shock also creates a transmitted ‘cloud shock’ that moves into the cloud and crushes it. The cloud shock propagates with a velocity $v_c \approx (\rho_i/\rho_c)^{1/2}v_s$, where ρ_i , ρ_c , and v_s are the density of the intercloud medium, the density of the cloud, and the shock velocity in the intercloud medium, respectively. A larger density contrast between the cloud and the intercloud medium causes a smaller velocity ratio of v_c/v_s , which helps the development of a shear flow, and consequently the Kelvin-Helmholtz instability at the cloud-intercloud interface. The Richtmyer-Meshkov instability powered by the impulsive acceleration takes place due to the impact of the shock wave on the upstream side of the cloud-intercloud surface. When the cloud shock exits the cloud, a rarefaction wave moves back into the cloud and causes expansion. This acceleration leads to the Rayleigh-Taylor instability on the upstream side of the cloud. The combined instabilities lead to the destruction of the cloud on a timescale of several times of the cloud-crushing time, $t_{cc} = R_c/v_c$.

The clump-young supernova remnant interaction is more complicated than the cloud-blast wave interaction because of the structure of the intershock structure, including the pre-existing large scale instability. The most important factor measuring the crushing strength of a cloud-shock interaction is the impact area per unit mass, which is inversely proportional to the initial density contrast, $\chi = \rho_c/\rho_i$. We have explored the evolution of a single clump, varying its size, density contrast, and initial impact time with the reverse shock. We examined four initial impact times, with the clump density contrast ranging between 3 and 100, and the clump size a_0 (as a fraction of the intershock width) below 1/3 (Table 1). We estimate the size of the Tycho X-ray knots to be about 1/5 the intershock width, although this is uncertain because the clumps are poorly resolved and we see only shocked parts of the clumps. For a size below 30% of the intershock width at the corresponding interaction time, we found that (a) an early clump initiated at $t' = 0.011$ must have a density contrast $\chi \gtrsim 10$ to cause a protrusion on the remnant outline; a clump with $\chi = 30$ causes a protrusion but the effect would have subsided long before the present epoch for Tycho; (b) a clump initiated at $t' = 0.22$ with $\chi = 50$ has a bulging effect on the remnant outline, but the outline returns to spherical symmetry by $t' = 1$; (c) a later clump initiated at $t' = 0.86$ with $\chi = 100$ is not dense enough to reach the forward shock at present epoch $t' = 1.6$ for Tycho. A light clump with $\chi = 3$ develops vorticity when encountering the reverse shock and is quickly destroyed.

Figs. (8) and (8) show the interaction with a single clump for $\chi = 100$ and two different interaction times. After passing through the reverse shock, the cloud gradually became flattened and curved like a crescent. Material streamed out from the horns of the crescent; the ram pressure difference between the axis and the side of the cloud drove the mass loss. The pressure near the cloud axis was higher because of the additional ram pressure on the front face of the clump. At the rear of the clump the flow became turbulent and left a trail of vortices. The clump expanded laterally as it approached the forward shock. The front of the clump snowplowed the material

ahead. The forward shock wave was distorted and a bulge formed. The material on the shock front became distributed into two lumps that gradually receded from each other. As the expansion of the supernova remnant continued, the bulge as well as the crescent clump immediately behind it lost their identities. Even a clump with $\chi = 100$ could not penetrate the forward shock when initiated at a later time (Fig. 8), but snowplowed the material ahead and caused a protrusion.

The velocity of a shocked clump is determined by the drag of the surrounding material. A shocked clump becomes comoving with the postshock flow in approximately the time that the cloud sweeps up a column density of intercloud gas equal to its initial column density. The drag time is proportional to $t_{drag} \sim \chi^{1/2} t_{cc}$, so that a denser clump travels faster in the remnant. The lateral expansion of a shocked clump into a crescent shape increases the cross section area and the drag, significantly decelerating the clump.

For an exponential density profile of the ejecta, the clump evolution depends on the time of clump interaction because of the evolution of the supernova remnant. An earlier clump requires less density contrast to have a protrusion effect on the remnant outline (Fig. 8). Early interactions give the clump a crescent shape without the action of the Rayleigh-Taylor instability on the clump’s front because the higher flow velocity in the remnant delays the rarefaction wave traveling back upstream as the cloud-shock exits the clump. Later clumps tend to develop instabilities on the clump surface. The exponential model gives a larger velocity difference and a larger density difference between the ejecta and the reverse shock front at earlier epochs. The early clumps rapidly move into a lower density medium and are thus more robust, for a given value of χ .

For $n_o = 0.8 \text{ cm}^{-3}$, $E = 10^{51} \text{ ergs}$, and $M = 1.4 M_\odot$ (DC98), Tycho’s remnant has $t' = 1.6$ at its present age of 427 years. If this model applies and the knots are in undecelerated motion, they must have crossed the reverse shock front at $t' \approx 1.2$. This places Tycho in the regime where $\chi \gtrsim 100$ is required.

In addition to the isolated knots, we considered groups of clumps. The Ni bubble process is likely to create a shell of clumpy ejecta and, as discussed in § 6, the observations of ejecta in Tycho’s remnant suggest that widespread clumpiness may be present. In Fig. (8) we show two simulations with multiple clumps. In the top one, there is one band of clumps and in the second, there are two bands. The evolution of each forward clump is similar to that in the isolated clump case, but they combine to push the forward shock wave to larger radius. The ejecta move out to a relatively large radius, as may be required in Tycho’s remnant.

6. THE REMNANT OF TYCHO’S SUPERNOVA

As discussed in § 1, Tycho’s supernova was likely to be of Type Ia. The expansion rate of the remnant has been measured in the radio, giving an expansion parameter $m = 0.47 \pm 0.05$ (Strom, Shaver, & Goss 1982), 0.462 ± 0.024 (Tan & Gull 1985), and 0.471 ± 0.028 (Reynoso et al. 1997). The optical filament yields an expansion parameter of 0.39 ± 0.01 (Kamper & van den Bergh

1978), close to the adiabatic blast wave case. The slight discrepancy in these measurements can be explained by sampling variance; the optical measurement samples only the densest regions where the emissivity is the highest. HI observations do indicate a higher surrounding density to the NE (Reynoso et al. 1999). These radio expansion values indicate a global pre-Sedov stage and exclude a surrounding circumstellar medium, which would give an expansion parameter ~ 0.7 (Chevalier 1982b; DC98). The exponential model is successful in reproducing the observed shock position and deceleration of Tycho’s remnant. At Tycho’s present age of 427 years ($t' = 1.7$) the model places the reverse shock and the forward shock at radii of 2.08 pc ($r' = 0.98$) and 3.09 pc ($r' = 1.45$), while they decelerate with expansion parameters of $m = 0.15$ and $m = 0.47$, respectively.

The radio observations of Tycho by VLA by Reynoso et al. (1997) show that the NE and particularly the adjacent SE parts protrude from the circular outline. The SE protrusion corresponds to the two X-ray knots. Near the sharp NE edge, Velázquez et al. (1998) note the presence of regularly spaced structure. The spatial regularity is interpreted by Velázquez et al. as Rayleigh-Taylor fingers still in the linear regime with a mode $l \sim 30$; they attribute the preferred wavenumber to the effects of viscosity. However, the importance of viscosity is uncertain because magnetic fields can inhibit its effect. We believe that a linear regime for the Rayleigh-Taylor instability is unlikely. Regardless of the supernova density model, the shock front has expanded by a sufficiently large factor to allow the instabilities to evolve to their saturated phase if there are initial perturbations with amplitude $\gtrsim 1\%$.

The regular structure observed in the radio image by Velázquez et al. (1998) is suggestive of a Rayleigh-Taylor instability, but there are problems with this interpretation in the context of our models. One is that at $t' = 1.6$, the region occupied by the unstable ejecta does not extend beyond 85 % of the remnant radius. The structure observed by Velázquez et al. is typically at a larger radius and in fact extends to the edge of the remnant. Another problem is that the instability at this late stage does not have a clear regular finger structure in our models, but is dominated by vortex rings with an irregular distribution. The large radius of the structure suggests that it may be connected to perturbations in the surrounding medium as opposed to the ejecta. However, the outer outline of the shock front is smooth on the scale of the structure, as imaged at both optical and radio wavelengths. In addition, the X-ray image of Tycho’s remnant (e.g., Vancura et al. 1995), which is dominated by line emission, shows strong emission at a large fractional radius. Because the image is likely to be dominated by emission from the ejecta (Vancura et al. 1995; Hwang & Gotthelf 1997), the evidence is that the outer structure is related to the ejecta.

We believe that a solution to this problem is indicated by the presence of the X-ray knots with undecelerated motion. Two knots are clearly observed in one section, but it is likely that they represent a more widespread phenomenon. We suggest that there was a spherical shell of clumpy ejecta at a velocity $\sim 6,000 - 8,000 \text{ km s}^{-1}$ in the freely expanding ejecta that gives rise to the clumpy structure. Kane et al. (1999) previously suggested that the radio structure observed in Tycho near the forward shock wave may be related to nonlinear density variations in the freely expanding ejecta. There are reasons to believe that the clumps are restricted to a region of the

ejecta and not spread through all velocities. First, the deceleration parameter measured at X-ray wavelengths is significantly larger than that measured at radio or optical wavelengths (Hughes 1997). If the clumps are widespread, they should come and go in a band that expands as does the emission at lower wavelengths. However, a band of clumps could give the observed difference in deceleration parameters. Another reason is that in SN 1006, the Fe II absorption line profiles are consistent with a distribution of gas at velocities $\lesssim 5,000 \text{ km s}^{-1}$ like that in the W7 model (Fesen et al. 1988), which has an approximately exponential density distribution. The Si line shows absorption at redshifted velocities $3,000 - 7,000 \text{ km s}^{-1}$, which can be attributed to moderately high velocity Si interacting with the surrounding medium. There is no blueshifted Si absorption. The data are consistent with the picture of smoothly distributed Fe on the inside, outside of which is Si gas that may be clumpy.

The presence of a band of clumps is expected in the Ni bubble scenario for clump formation (see § 2). One prediction of this model is that the outer ejecta emission should be very clumpy when observed at high X-ray resolution (see Fig. (8)). In addition to this component, there should be emission from a smaller radius, near the reverse shock front. This emission should be representative of lower density, higher temperature gas. We believe that the emission in the Fe K line, which is at a smaller radius (Hwang & Gotthelf 1997), is primarily from gas close to the reverse shock wave. This gas should have some structure because of the earlier instabilities, but much less than the outer clumpy ejecta.

Our computations showed that in order for knots to survive to close to the outer shock wave, they must have an initial density contrast with respect to their surroundings of ~ 100 . Hwang et al. (1998) in fact find that the ionization time ($n_e t$, where t is the time since the gas was heated) is 100 times larger for Si than for Fe, based on line emission from the entire remnant. The time since heating should be comparable for the two elements, so this result is consistent with the Si being primarily in shocked clumps (created outside the Ni bubble) and the Fe primarily in interclump gas (inside the Ni bubble). However, the situation is complicated by the fact that there is evidence for some Fe in knots, which we argue had a nonradiogenic origin (e.g., ^{54}Fe). In addition, we estimated in § 2 that $\sim 0.13 M_\odot$ of Si could be swept into a shell around the Ni bubble, so there could be some Si emission from the ejecta that is not clumped. Investigation of these issues will require spatially resolved X-ray spectroscopy, as will be possible with the *Chandra* and *XMM* observatories.

7. IMPLICATIONS FOR TYPE Ia SUPERNOVA MODELS

One result from observations of the Type Ia remnants is a lower limit on the velocity of Si in the explosion. For Tycho’s supernova, there is an undecelerated knot of Si moving at $8,300(D/2.5 \text{ kpc}) \text{ km s}^{-1}$, where D is the distance. In SN 1006, there is Si freely expanding with a minimum velocity in the range $5,600 - 7,000 \text{ km s}^{-1}$. In both of these cases, the velocities appear to be less than the minimum velocity of the Si-dominant layer in the W7 deflagration model, about $10,000 \text{ km s}^{-1}$ (Thielemann et al. 1986). However, if these are the remnants of

subluminous supernovae, the W7 model may not be the appropriate one. Also, the initial burning front is unlikely to be precisely spherically symmetric, so that some material that has not burned to ^{56}Ni may lag behind.

Our most significant results involve the evidence for clumping in Type Ia supernovae. We have found that density contrasts $\gtrsim 100$ are necessary to reproduce the large radius of X-ray emitting clumps and their velocities. A plausible mechanism for the formation of the clumps is the action of an expanding Ni bubble, although calculations of this process have not yet shown that such large compressions are feasible. We estimate that $\sim 0.1 M_{\odot}$ of matter can be swept into clumps around the Ni bubble. For the two undecelerated X-ray emitting clumps in Tycho’s remnant, Hughes (1997) estimates a mass of order $0.002 M_{\odot}$ for the Si + S clump and $0.0004 M_{\odot}$ for the Fe clump, so there can be many comparable clumps. The presence of Fe in a clump requires that it have a non-radioactive origin. The 1-dimensional calculations of nucleosynthesis associated with the W7 Type Ia model (Thielemann et al. 1986; Iwamoto et al. 1999) show that ^{54}Fe is present along with Si and S in the region immediately outside of the ^{56}Ni region. However, the ^{54}Fe does not dominate the composition, unlike what is indicated by the observations of the Fe clump in Tycho. The central region of the W7 model is composed of stable ^{56}Fe and ^{54}Fe , but this gas is at too low a velocity to be compatible with the Tycho clump. Thus, the synthesis of fast material dominated by non-radioactive Fe remains to be demonstrated.

8. CONCLUSIONS

We used 2-D hydrodynamical simulations in spherical polar coordinates to investigate instabilities and clumpiness in a Type Ia supernova remnant. We adopted an exponential density profile for the smooth supernova ejecta and a constant density for the surrounding (interstellar) medium. The exponential density profile gives the best general approximation for the supernova ejecta in detailed explosion models, as opposed to a power law density profile for which self-similar solutions are available. The region between the forward shock in the interstellar medium and the reverse shock in the ejecta is Rayleigh-Taylor unstable. An initial perturbation grows to nonlinear strength, develops an increasing characteristic wavelength, and fades as the remnant evolves to the Sedov blast wave regime. The characteristic Rayleigh-Taylor mushroom caps are replaced by vortex rings from the Kelvin-Helmholtz instability, and turbulence appearing in vortices remains dominant throughout the rest of the evolution. In these late phases, the depletion of the kinetic energy in the inner ejecta as the ejecta density profile continually weakens the acceleration needed to power the Rayleigh-Taylor instability. A sequence of simulations with increasing grid resolution shows the Rayleigh-Taylor fingers become increasingly slender and sharp and tend to bend, limited only by the grid resolution.

The structure that is formed as a result of the Rayleigh-Taylor instability is decelerated and is confined to a region $\lesssim 85\%$ of the remnant radius for a remnant with the dynamical age of Tycho’s remnant. These properties are not consistent with the knots observed in Tycho’s remnant. We

thus considered a clump in the diffuse supernova ejecta with the aim of reproducing the properties of the the SE X-ray knots and the related protrusion on the forward shock outline. In the clump-shock interaction, the density contrast, clump size, and time of initiation of the interaction are the major factors. Ram pressure stripping gives rise to a core-plume structure and a strong Kelvin-Helmholtz instability in the downstream region. The Rayleigh-Taylor instability develops on the clump’s upstream side, which facilitates fragmentation of the clump. The clump causes a bulge on the remnant outline as the ram pressure pushes material ahead. The bulge eventually disappears as the clump is fragmented and swept back. Punching through the forward shock does not occur for our simulation with conditions like those in Tycho’s remnant, even for the case of a clump with an initial density contrast of 100. Clump interaction in the early phases of the remnant evolution are more likely to distort the forward shock front because of the larger density contrast between the ejecta and the interstellar medium.

The two X-ray clumps to the SE in Tycho are probably not alone. In fact, we find that the large radial position of most of the ejecta emission suggests that much of the emission is from clumps. If it were not in clumps, it could not extend to the observed radius. We thus suggest that the undecelerated knots are at the high column density end of a spectrum of knot properties. The required knot compression factor, up to ~ 100 , is not a natural result of existing Type Ia supernova models. We suggest that the expansion of a radioactive Nickel bubble is responsible for the compression of the knots. The compression factor is larger than that found in existing calculations, but it is possible that radiative transfer effects during the final stages of the Ni bubble expansion can lead to enhanced compression. The Ni bubble interpretation has the implication that Fe clumps, which are observed, cannot have been synthesized as ^{56}Ni . They must have a non-radiogenic origin, such as ^{54}Fe . The synthesis of high velocity matter in which ^{54}Fe is the dominant component has yet to be shown in computations of nucleosynthesis.

In addition to these suggested theoretical investigations, advances can be expected on the observational front. Spatially resolved X-ray spectra of Type Ia supernova remnants, as is possible with the *Chandra* and *XMM* observatories, will be valuable for showing whether our picture of ejecta clumps is valid. We predict that the outer ejecta emission in Tycho’s remnant has a clumpier structure than the inner emission observed in the Fe K line.

C.-Y. Wang thanks John Blondin and John Hawley for their assistance with the numerical simulations, and Fred Lo and Academia Sinica for providing their facilities. R.A.C. is grateful to Vikram Dwarkadas, Peter Höflich, Phil Pinto, and Craig Wheeler for useful discussions and correspondence. The computations were carried out on the Cray T90 of NPACI, and the IBM SP2 at University of Virginia. Support for this work was provided in part by NASA grant NAG5-8232.

REFERENCES

- Baade, W. 1945, *ApJ*, 102, 309
- Basko, M. 1994, *ApJ*, 425, 264
- Branch, D., Doggett, J. B., Nomoto, K., & Thielemann, F.-K. 1985, *ApJ*, 294, 619
- Chevalier, R. A. 1981a, *ApJ*, 246, 267
- Chevalier, R. A. 1981b, *Fund. of Cosmic Phys.*, 7, 1
- Chevalier, R. A. 1982a, *ApJ*, 258, 790
- Chevalier, R. A. 1982b, *ApJ*, 259, L85
- Chevalier, R. A. 2000, in *Astronomy with Radioactivities*, ed. R. Diehl (Garching: MPI), in press
- Chevalier, R. A., Blondin, J. M., & Emmering, R. T. 1992, *ApJ*, 392, 118.
- Dwarkadas, V. V. 2000, *ApJ*, submitted
- Dwarkadas, V. V., & Chevalier, R. A. 1998, *ApJ*, 497, 807 (DC98)
- Fesen, R. A., Wu, C.-C., Leventhal, M., & Hamilton, A. J. S. 1988, *ApJ*, 327, 164
- Fryxell, B., Müller, E., & Arnett, W. D. 1991, *ApJ*, 367, 619
- Hamilton, A. J. S., Sarazin, C. L., & Szymkowiak, A. E. 1986, *ApJ*, 300, 713
- Hamilton, A. J. S., Fesen, R. A., Wu, C.-C., Crenshaw, D. M., & Sarazin, C. L. 1997, *ApJ*, 482, 838
- Harkness, R. P. 1991, in *SN 1987A and Other Supernovae*, ed. I. J. Danziger & K. Kjær (Garching: ESO), 447
- Höflich, P. 2000, priv. commun.
- Höflich, P., & Khokhlov, A. 1996, *ApJ*, 457, 500
- Höflich, P., Khokhlov, A. M., & Wheeler, J. C. 1995, *ApJ*, 444, 831
- Hughes, J. P. 1997, in *X-Ray Imaging and Spectroscopy of Cosmic Hot Plasmas*, ed. F. Makino and K. Mitsuda (Tokyo: Universal Academy Press), 359
- Hwang, U., & Gotthelf, E. V. 1997, *ApJ*, 475, 665
- Hwang, U., Hughes, J. P., & Petre, R. 1998, *ApJ*, 497, 833

- Iwamoto, K., Brachwitz, F., Nomoto, K., Kishimoto, N., Umeda, H., Hix, W. P., & Thielemann, R.-K. 1999, *ApJS*, 125, 439
- Jun, B.-I., & Jones, T. W. 1999, *ApJ*, 511, 774
- Jun, B.-I., & Norman, M. L. 1996, *ApJ*, 465, 800
- Jun, B.-I., & Norman, M. L. 1996b, *ApJ*, 472, 245
- Kane, J., Drake, R. P., & Remington, B. A. 1999, *ApJ*, 511, 335
- Kane, J., Arnett, D., Remington, B. A., Glendinning, S. G., Bazán, G., Müller, E., Fryxell, B. A., & Teyssier, R. 2000, *ApJ*, 528, 989
- Kamper, K. W., & van den Bergh, S. 1978, *ApJ*, 224, 851
- Khokhlov, A. 1991, *A&A*, 245, L25
- Klein, R. I., McKee, C. F., & Colella, P. 1994, *ApJ*, 420, 213
- Li, H., McCray, R., & Sunyaev, R. A. 1993, *ApJ*, 419, 824
- Livne, E., & Arnett, D. 1995, 452, 62
- Mazzali, P. A., Chugai, N., Turatto, M., Lucy, L. B., Danziger, I. J., Cappellaro, E., Della Valle M., & Benetti, S. 1997, *MNRAS*, 284, 151
- bibitem[Fryxell et al.(1991)]fma91 Müller, E., Fryxell, B., & Arnett, D. 1991, *A&A*, 251, 505
- Nomoto, K., Thielemann, F.-K., & Yokoi, K. 1984, *ApJ*, 286, 644
- Raymond, J. C. 1984, *ARA&A*, 22, 75
- Reynoso, E. M., Moffett, D. A., Goss, W. M., Dubner, G. M., Dickel, J. R., Reynolds, S. P., & Giacani, E. B. 1997, *ApJ*, 491, 816
- Reynoso, E. M., Velázquez, P. F., Dubner, G. M., & Goss, W. M. 1999, *AJ*, 117, 1827
- Schneider, M., Dimonte, G., & Remington, B. A. 1998, *Phys. Rev. Lett.*, 80, 3507
- Schaefer, B. E. 1996, *ApJ*, 459, 438
- Seward, F., Gorenstein, P., & Tucker, W. 1983, *ApJ*, 266, 287
- Stone, J., & Norman, M. 1992, *ApJS*, 80, 753.
- Strom, R. G., Goss, W. M., & Shaver, P. A. 1982, *MNRAS*, 200, 473.
- Tan, S. M., & Gull, S. G. 1985, *MNRAS*, 216, 949

- Thielemann, F.-K., Nomoto, K., & Yokoi, K. 1986, *A&A*, 158, 17
- Truelove, K., & McKee, C. F. 1999, *ApJS*, 120, 299
- van den Bergh, S. 1993, *ApJ*, 413, 67
- Vancura, O., Gorenstein, P., & Hughes, J. P. 1995, *ApJ*, 441, 680
- Velázquez, P. F., Gómez, D. O., Dubner, G. M., Giménez de Castro, G., & Costa, A., 1998, *A&A*, 334, 1060
- Whelan, J., & Iben, I., Jr. 1973, *ApJ*, 186, 1007
- Woosley, S. E. 1988, *ApJ*, 330, 218
- Woosley, S. E., & Weaver, T. A. 1994, *ApJ*, 423, 371
- Wu, C.-C., Leventhal, M., Sarazin, C. L. & Gull, T. R. 1983, *ApJ*, 269, L5
- Wu, C.-C., Crenshaw, D. M., Hamilton, A. J. S., Fesen, R. A., Leventhal, M., & Sarazin, C. L. 1997, *ApJ*, 477, L53
- Xu, J., & Stone, J. M. 1995, *ApJ*, 454, 172

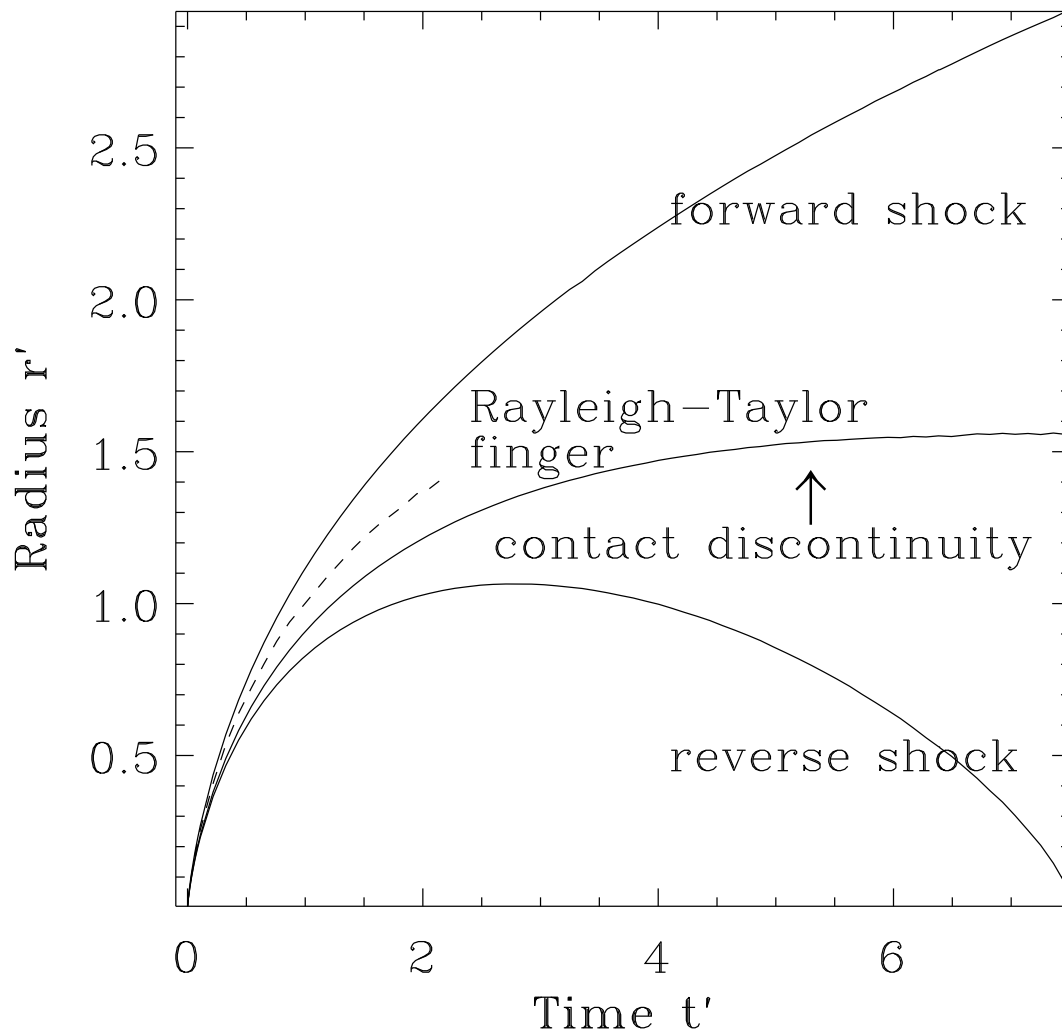


Fig. 1.— One-dimensional evolution of the forward shock, the contact discontinuity, and the reverse shock radius with time. The farthest position to which the Rayleigh-Taylor fingers stretch in two-dimensional simulations is also plotted. The time and radius use normalized units given in the text.

Fig. 2.— evo.gif

Series of density images illustrating the time evolution of the dynamical instability. The perturbation was imposed at $t' = 0.00054$ with 1% amplitude and an $l = 100$ mode of the spherical harmonic function. The grid has 500 radial zones by 2000 angular zones in 1/2 of a quadrant. The plots at early stages display the central 1000 angular zones in 1/4 of a quadrant, while the plots shown for later stages display 1/2 of a quadrant. The contour levels are exponentially spaced between the lowest value and the highest one sampled in the grid domain.

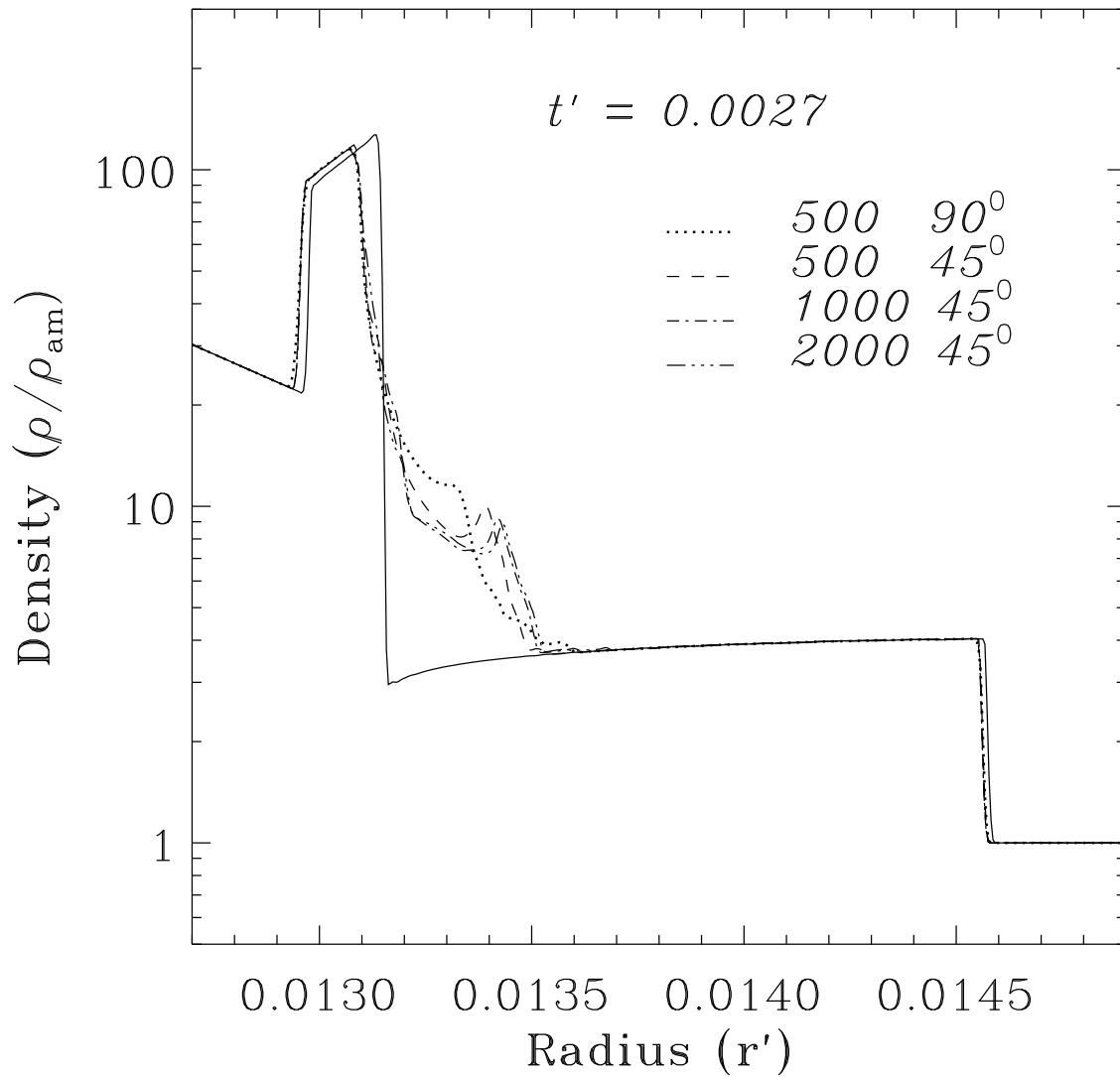


Fig. 3.— Angle-averaged two-dimensional density distribution overplotted on the one-dimensional unperturbed solution in varying grid resolutions with $l = 100$ and 1% perturbing amplitude. The plot is at an early dynamical stage: $t' = 0.0027$.

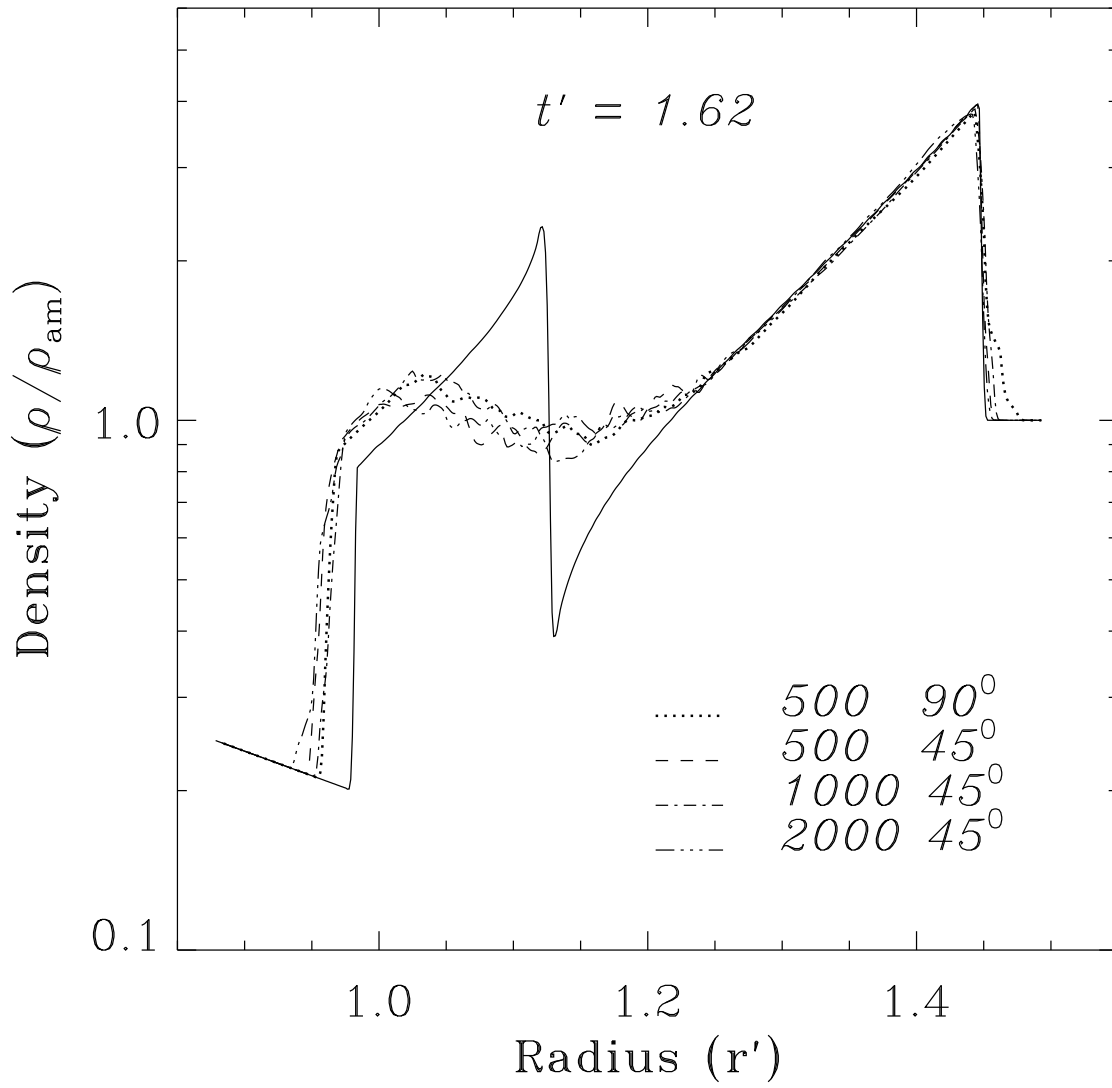


Fig. 4.— Angle-averaged two-dimensional density distribution. The plot is at $t' = 1.62$, corresponding to the present age of Tycho's remnant.

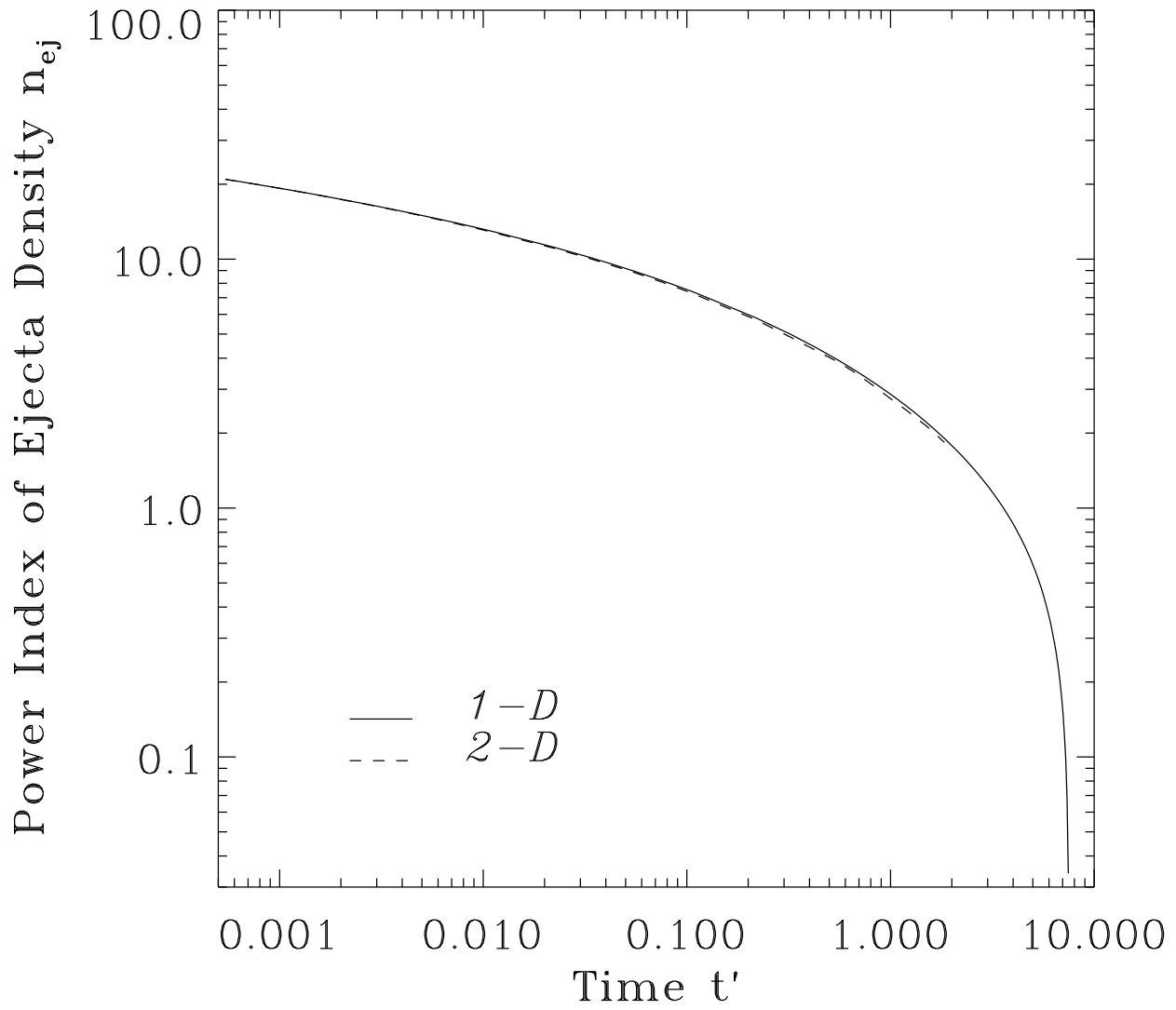


Fig. 5.— Time evolution of the power law index of the ejecta density profile immediately below the reverse shock front from both the one-dimensional and two-dimensional runs.

Fig. 6.— resol.gif

Series of density contours with varying resolutions for four epochs: $t' = 0.0016, 0.0027, 0.011,$ and 0.11 . The lowest resolution uses 200 angular zones on $1/2$ of a quadrant and the highest uses 2000 zones on $1/2$ of a quadrant. The top two low resolution plots exhibit the same dominant modes on $1/2$ of a quadrant, growing from the initial perturbation modes $l = 100$ and $l = 50$. The other plots are shown on $1/4$ of a quadrant. All of the plots use a 10% perturbing amplitude.

Fig. 7.— G0mplt.gif

Snapshots of a clump in the ejecta expanding into the shocked region. The clump was initiated at $t' = 0.207$, with an initial density contrast $\chi = 100$ and a size $a_0 = 1/8$. The clump becomes crescent shaped and causes a protrusion in the forward shock front. The grid has 500 radial by 500 angular zones on $1/2$ of a quadrant.

Fig. 8.— k2mplt.gif

Snapshots of a clump with an initial density contrast $\chi = 100$ and a size $a_0 = 1/6$ in the ejecta expanding into the shocked region. The interaction was initiated at $t' = 0.866$. The Rayleigh-Taylor instability can be seen on the clump's downstream side. The grid has 500 radial by 500 angular zones on $1/2$ of a quadrant.

Fig. 9.— band.gif

Snapshots of multiple clumps with a initial density contrast $\chi = 50$ and a size $a_0 = 0.15$ in the ejecta expanding into the shocked region. The interaction was initiated at $t' = 0.866$. The grid has 500 radial by 500 angular zones on $1/2$ of a quadrant. The top plot has one row of clumps and the bottom has two rows.

Table 1: Clump Simulation Parameters

t' ^a	ρ_c ^b	R_{rs} ^c	R_{fs} ^d	dR ^e
0.011	15.5	0.042	0.048	0.006
0.217	2.03	0.797	0.958	0.161
0.866	0.580	1.70	2.26	0.478
1.24	0.315	1.93	2.70	0.768

^astarting time of the clump-reverse shock interaction

^bclump density for $\chi = 1$, normalized to the unshocked ISM

^cnormalized radius of the reverse shock

^dnormalized radius of the forward shock

^enormalized intershock width

This figure "G0mplt.gif" is available in "gif" format from:

<http://arxiv.org/ps/astro-ph/0005105v1>

This figure "band.gif" is available in "gif" format from:

<http://arxiv.org/ps/astro-ph/0005105v1>

This figure "evo.gif" is available in "gif" format from:

<http://arxiv.org/ps/astro-ph/0005105v1>

This figure "k2mplt.gif" is available in "gif" format from:

<http://arxiv.org/ps/astro-ph/0005105v1>

This figure "resol.gif" is available in "gif" format from:

<http://arxiv.org/ps/astro-ph/0005105v1>